The Astrophysical Journal, 906:68 (10pp), 2021 January 10 https://doi.org/10.3847/1538-4357/abcaa0

Properties of Galaxies in Cosmic Filaments around the Virgo Cluster

Youngdae Lee[1], Suk Kim[1], Soo-Chang Rey[1], and Jiwon Chung[2]
[1] Department of Astronomy and Space Science, Chungnam National University, Daejeon 34134, Republic of Korea; hippo206@gmail.com, screy@cnu.ac.kr
[2] Korea Astronomy and Space Science Institute 776, Daedeokdae-ro, Yuseong-gu, Daejeon 34055, Republic of Korea
Received 2020 July 5; revised 2020 November 1; accepted 2020 November 13; published 2021 January 11

Abstract

We present the properties of galaxies in filaments around the Virgo cluster with respect to their vertical distance from the filament spine using the NASA–Sloan Atlas catalog. The filaments are mainly composed of low-mass, blue dwarf galaxies. We observe that the $g - r$ color of galaxies becomes blue and stellar mass decreases with increasing vertical filament distance. The galaxies were divided into higher-mass ($\log(h^2 M_*/M_\odot) > 8$) and lower-mass ($\log(h^2 M_*/M_\odot) \leqslant 8$) subsamples. We also examine the distributions of $g - r$ color, stellar mass, Hα equivalent width (EW(Hα)), near-ultraviolet (NUV) $- r$ color, and H I fraction of the two subsamples with the vertical distance. The lower-mass galaxies exhibit a negative $g - r$ color gradient, whereas higher-mass galaxies have a flat $g - r$ color distribution. We observe a negative EW(Hα) gradient for higher-mass galaxies, whereas lower-mass galaxies show no distinct EW(Hα) variation. In contrast, the NUV $- r$ color distribution of higher-mass galaxies shows no strong trend, whereas the lower-mass galaxies show a negative NUV $- r$ color gradient. We do not see clear gradients of H I fraction in either the higher- or lower-mass subsample. We propose that the negative color and stellar mass gradients of galaxies can be explained by mass assembly from past galaxy mergers at different vertical filament distances. In addition, galaxy interactions might be responsible for the contrasting features of EW(Hα) and NUV $- r$ color distributions between the higher- and lower-mass subsamples. The distributions of H I fraction of the two subsamples suggest that the processes of ram pressure stripping and gas accretion may be ignored in the Virgo filaments.

Unified Astronomy Thesaurus concepts: Dwarf galaxies (416); Galaxy interactions (600); Galaxy evolution (594); Large-scale structure of the universe (902)

1. Introduction

In the framework of hierarchical structure formation in the standard cold dark matter universe, the buildup of galaxy clusters is characterized by the accretion of galaxies into higher-density cluster environments through filamentary structures (Bond et al. 1996; Springel et al. 2005). It has been proposed that the filament environment around galaxy clusters is closely linked to galaxy evolution in terms of the subject of "preprocessing" (Fujita 2004), where properties of galaxies may already have been altered before they enter galaxy clusters (Zabludoff et al. 1996; De Lucia et al. 2012; Mahajan 2013; Cybulski et al. 2014). Therefore, filaments are ideal places for the investigation of the physical processes that control the transitioning of galaxies from less dense environments to clusters.

Recently, the specific role of preprocessing in filaments has been extensively explored in different surveys. In particular, there is a growing body of observational evidence indicating that the properties of galaxies (e.g., color, mass, red galaxy fraction, and star formation rate) change as a function of their distance from the filament spine (e.g., Alpaslan et al. 2016; Martínez et al. 2016; Chen et al. 2017; Kuutma et al. 2017; Malavasi et al. 2017; Kraljic et al. 2018; Mahajan et al. 2018; Bonjean et al. 2020; Luber et al. 2019; Sarron et al. 2019). Galaxies close to filaments show a tendency to have redder colors, lower Hα emission-line equivalent width (EW(Hα)), and a higher fraction of early- to late-type galaxies, indicating that the efficiency of star formation quenching varies with distance from filaments. Furthermore, higher-mass galaxies are preferentially located closer to filaments. These observational results support the idea that galaxies could be effectively preprocessed in a moderately dense filament environment.

Several environmental effects are proposed as possible physical mechanisms that could be responsible for the galaxy preprocessing in filaments. Merger and tidal interaction between galaxies are expected to be a prevailing process in the filament environment (Darvish et al. 2015; Malavasi et al. 2017; Kraljic et al. 2018; Mahajan et al. 2018). In addition, stripping of gas within galaxies in filaments can be caused by a warm–hot intergalactic medium (WHIM, 10^5 K $< T <$ 10^7 K, e.g., Benítez-Llambay et al. 2013; see also Tonnesen et al. 2007 for ram pressure stripping in the cluster periphery) within filaments. Another process is that galaxies moving along the filaments can accrete cold gas from the intrafilament medium (Kereš et al. 2005; Sancisi et al. 2008; Darvish et al. 2015; Kleiner et al. 2017).

To date, most observational studies of filaments have concentrated on massive galaxies with $>10^{10} M_\odot$ mainly because filaments are only defined at intermediate and high redshifts. On the other hand, since low-mass ($<10^9$ $M_\odot$) dwarf galaxies, with low binding energies, are more susceptible to even weak perturbations than massive galaxies, they are a better tool to probe the details of the multiple processes occurring in filaments that can affect the properties of filament galaxies. Recently, Kim et al. (2016) identified seven filaments around the Virgo cluster, the nearest rich and dynamically young cluster (Aguerri et al. 2005), in which the majority of galaxies are faint dwarfs ($M_B > -19$ mag; ~88% of the total sample). Therefore, Virgo filaments are prime targets for detailed investigations of the physical processes affecting galaxy properties in a filament environment.

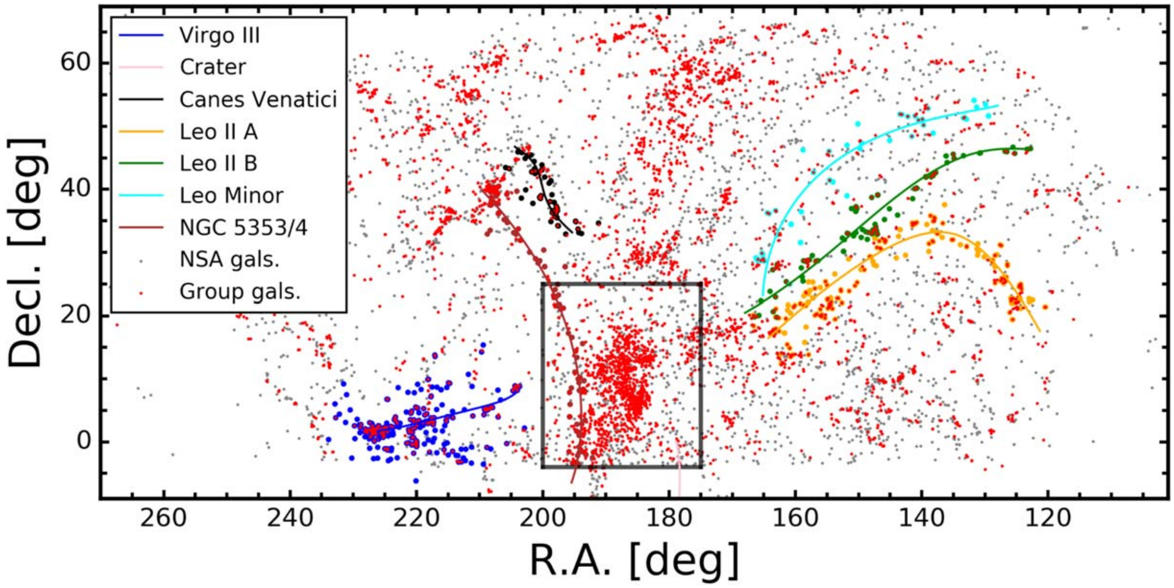

Figure 1. Spatial distribution of galaxies around the Virgo filaments in the equatorial coordinate system. Colored curves are spines of seven filaments identified by Kim et al. (2016) and colored circles are selected member galaxies that belong to the filaments. NSA galaxies at $z < 0.014$ and group galaxies are denoted by gray dots and red circles, respectively. The large rectangular box is the region of the Virgo cluster covered by the Extended Virgo Cluster Catalog (EVCC, Kim et al. 2014). In our study, we only consider galaxies that do not belong to galaxy groups (colored circles without red dots).

In response to this situation, in this work we explore the impact of the filaments in the vicinity of the Virgo cluster on the properties of filament galaxies using the photometric and spectroscopic data of the Sloan Digital Sky Survey (SDSS), Galaxy Evolution Explorer (GALEX) ultraviolet (UV) data, and neutral hydrogen (H I) gas data of the Arecibo Legacy Fast ALFA (ALFALFA) blind survey. In Section 2, we describe the basic data of galaxies in and around the Virgo filaments. Section 3 describes the selection of member galaxies in filaments. In Section 4, we show our results on the variations of galaxy properties (optical and UV colors, mass, central and global star formations, and H I gas content) as a function of the vertical filament distance. A discussion on physical processes in filaments is given in Section 5. Finally, we summarize our results in Section 6. Throughout this paper, we assume $h = H_0/(100\,\mathrm{km\,s^{-1}\,Mpc^{-1}})$, the matter density $\Omega_m = 0.27$, and the dark energy density $\Omega_\lambda = 0.73$ (Komatsu et al. 2011).

2. Data

Our basic sample is drawn from galaxies at $z < 0.014$ in and around the Virgo filaments from the NASA–Sloan Atlas (NSA) catalog. In order to identify galaxies associated with galaxy groups residing on filaments, we make use of our sophisticated galaxy group catalog (Y. Lee et al. in preparation). This is constructed for SDSS galaxies in the redshift range $0.001 < z < 0.2$ with the use of friends-of-friends for group detection. We examined the radial velocity distribution of NSA galaxies as a function of the group-centric distance. In this distribution, we overplotted a spherically symmetric infall model using the measured velocity dispersion and virial radius of each group (Praton & Schneider 1994). We assigned NSA galaxies to group galaxies if they are bounded by the caustic curves of the infall model. Finally, we only selected galaxies that do not belong to groups in order to investigate how galaxies change their properties with varying distances from the filaments, avoiding contamination from member galaxies of groups located in filaments (e.g., Alpaslan et al. 2016; Bonjean et al. 2020). This allows us to study the galaxy evolution in a filament unaffected by local environmental effects occurring in groups (Robotham et al. 2013; Davies et al. 2015; Alpaslan et al. 2016).

Figure 1 shows the sky distribution of galaxies around the filaments. Gray dots indicate NSA galaxies at $z < 0.014$; different colored circles represent member galaxies belonging to different filaments (see Section 3), and red circles are the group galaxies. The spines of different filaments are plotted with curves of different colors. The Crater filament galaxies are excluded from our analysis since the NSA catalog does not cover most of this filament in the Southern Hemisphere.

3. Selection of Member Galaxies in Filaments

Since our study focuses on the properties of filament galaxies in the vertical direction from the filament spine, we need to define possible member galaxies belonging to each filament structure. In order to construct an accurate spatial distribution of galaxies in the NSA, we first converted the observed heliocentric radial velocities extracted from the NSA into velocities relative to the centroid of the Local Group using a method from Karachentsev & Makarov (1996). All NSA galaxies were then mapped in the supergalactic coordinate system (SGX, SGY, SGZ), which was converted from heliocentric radial velocities and positions (R.A. and decl.) of galaxies based on the assumption of a linear relationship between radial velocity and distance. We adopted the spines of filaments obtained by Kim et al. (2016), which are created by the three-dimensional third-order polynomial fitting of visually selected filament structures (see Kim et al. 2016 for details). We finally measured the three-dimensional vertical distances of galaxies (D_{ver}) from the filament spine in megaparsecs. In the case of the Virgo III filament, since it is contiguous to the Virgo cluster in the SGZ direction, we rejected galaxies within a distance of $1.5\,h^{-1}$ Mpc from the center of the supergalactic coordinate system in the SGZ direction to avoid contamination from cluster galaxies.

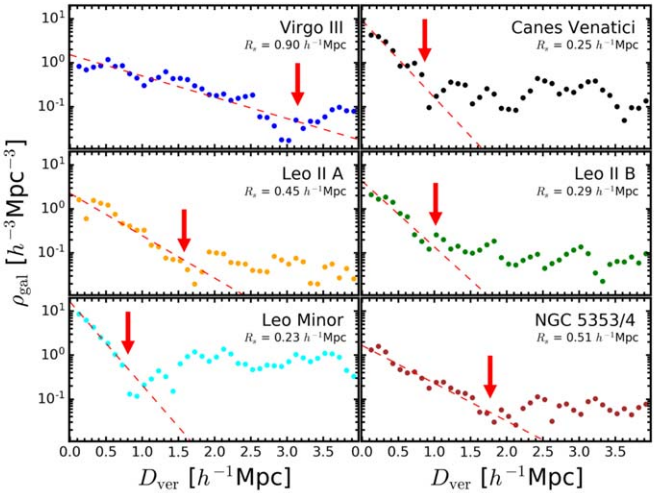

Figure 2. Profiles of galaxy number density of six filaments as a function of the vertical distance from the filament spine ($D_{\rm ver}$). Circles are observed number densities at different $D_{\rm ver}$ and dashed lines indicate the best-fit exponential models. In each panel, the scale length (R_s) of each filament is indicated and the filament membership criterion (i.e., within $3.5R_s$ from the filament spine) is presented as a red arrow.

Figure 2 presents profiles of galaxy number density ($\rho_{\rm gal}$) of each filament as a function of $D_{\rm ver}$. We define $\rho_{\rm gal}$ at $D_{\rm ver}$ as the number of galaxies in a cylindrical volume along the filament spine in the supergalactic coordinate system. $\rho_{\rm gal}$ was measured by the moving bin method with a bin size of $0.25\,h^{-1}$ Mpc and a step size of $0.1\,h^{-1}$ Mpc in the $D_{\rm ver}$ direction. The overall feature in all filaments is that $\rho_{\rm gal}$ systemically decreases from the filament spine to a certain $D_{\rm ver}$ and then shows no variation with increasing $D_{\rm ver}$. We have fitted the decreasing part of the observed $\rho_{\rm gal}$ distribution with an exponential function:

$$\rho_{\rm gal} = \rho_0 \exp(-D_{\rm ver}/R_s), \quad (1)$$

where ρ_0 and R_s are the central galaxy number density and scale length, respectively. The best-fit parameters are shown in Table 1 and the best-fit models are presented as red dashed lines in Figure 2. All R_s are found to be less than $1\,h^{-1}$ Mpc. Finally, we define member galaxies belonging to the filament as those within $3.5R_s$ from the filament spine. We note that $3.5R_s$ well represents the location of a local minimum density in the $\rho_{\rm gal}$ distribution (see red arrows indicating $3.5R_s$ in Figure 2). A total of 289 member galaxies are selected in six filaments.

For our analysis, we extracted photometric and spectroscopic parameters of member galaxies from the NSA; optical and UV magnitudes, stellar mass, and intensities of various emission lines (e.g., Hα, Hβ, [O III], [N II]). These parameters in the NSA are mainly derived from the SDSS optical data with the addition of the GALEX UV data.

4. Results

4.1. Stellar Mass Distribution and Color–Magnitude Diagram

The filaments around the Virgo cluster defined by Kim et al. (2016) are the nearest large-scale structures to us (∼14–41 Mpc), and mostly consist of faint dwarf galaxies ($M_B > -19$; ∼88% of the total sample). In Figure 3, we present the stellar mass (M_*) distribution of member galaxies in filaments. It is clear that most (87%) of our filament galaxies are lower-mass ones with $\log(h^2M_*/M_\odot) < 9$, in which the median and standard deviation are 7.7 and 0.6, respectively.

We examined the photometric completeness of our galaxy sample by fitting the conventional Schechter function (see Equation (2) of Vulcani et al. 2013) to the stellar mass distribution of higher-mass galaxies with $\log(h^2M_*/M_\odot) > 7.5$. We estimated the slope at the low-mass end ($\alpha = -1.34$) and the characteristic stellar mass ($\log(h^2M_*/M_\odot) = 10.47$) of the fitted mass function. Assuming this mass function is photometrically complete, we calculated the completeness of our filament galaxy sample at each mass bin, which is the number ratio between the fitted Schechter function and observed stellar mass distribution. The completeness of galaxy samples for $\log(h^2M_*/M_\odot) > 7$ and $\log(h^2M_*/M_\odot) < 7$ is found to be 84% and 4%, respectively. We found no significant change in our main results when we use only a relatively more complete sample with $\log(h^2M_*/M_\odot) > 7$. We henceforth utilized the total sample galaxies without taking completeness into consideration for our analysis.

Figure 4 shows the $g - r$ and near-ultraviolet (NUV) $- r$ color–magnitude diagrams (CMDs) of galaxies in filaments (blue circles). For comparison with galaxies in a denser environment, we also overplot galaxies in the Virgo cluster (black dots) based on the SDSS optical and GALEX UV photometry of the EVCC (Kim et al. 2014), adopting a distance

Table 1
Properties of Filaments

Name (1)	ρ_0 (h^{-3} Mpc^{-3}) (2)	R_s (h^{-1} Mpc) (3)	Length (h^{-1} Mpc) (4)	N (5)
Virgo III	1.51 ± 0.21	0.90 ± 0.07	12.39	92
Canes Venatici	9.09 ± 2.45	0.25 ± 0.03	7.23	26
Leo II A	2.26 ± 0.42	0.45 ± 0.05	18.91	57
Leo II B	4.27 ± 1.04	0.29 ± 0.04	16.96	34
Leo Minor	16.31 ± 4.46	0.23 ± 0.03	5.91	26
NGC 5353/4	1.66 ± 0.31	0.51 ± 0.05	23.22	54

Note. (1) Name of the filament. (2) Central galaxy number density of the exponential best-fit model. (3) Scale length of the exponential best-fit model. (4) Length of the filament in the SGX–SGY–SGZ plane. (5) Number of member galaxies that do not belong to groups.

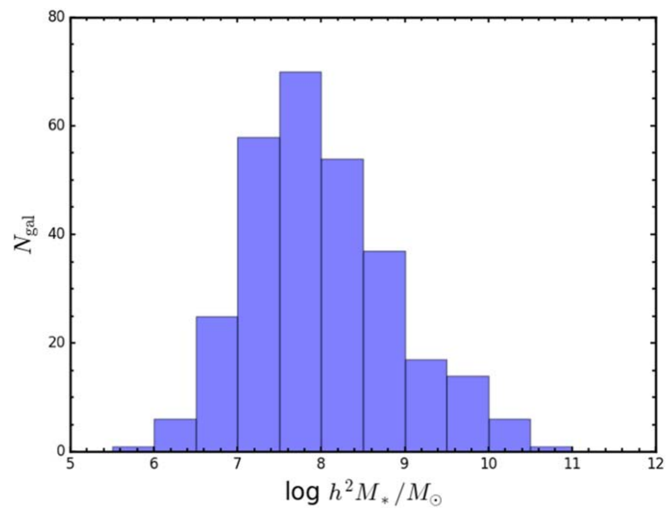

Figure 3. Stellar mass distribution of member galaxies in filaments.

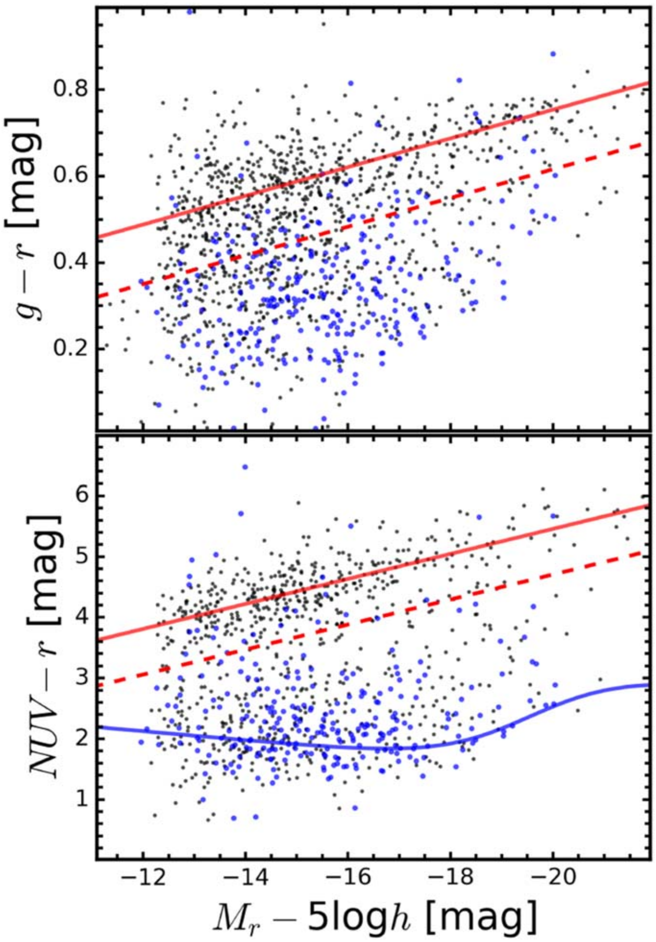

Figure 4. $g-r$ (top) and NUV $-$ r (bottom) CMDs of galaxies in filaments (blue circles). For comparison, galaxies in the Virgo cluster are also overplotted (black dots). The red solid lines represent the red sequence of the Virgo cluster and the red dashed lines are -3σ deviation from the red sequence. In the NUV $-$ r CMD, the blue curve indicates the blue cloud defined by Wyder et al. (2007).

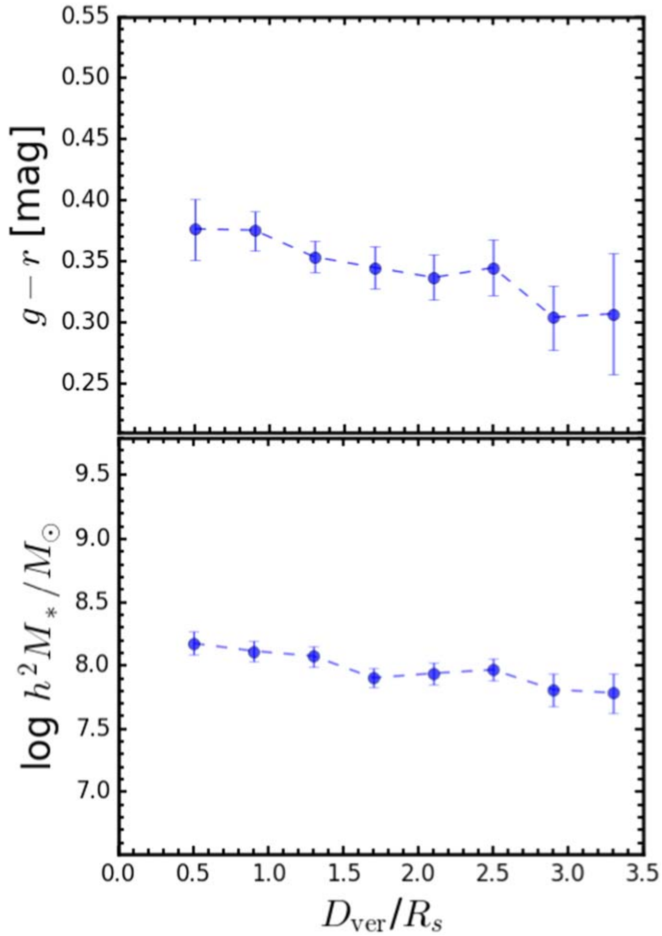

Figure 5. $g-r$ color (top) and stellar mass (bottom) vs. scaled vertical distance from the filament spine ($D_{\rm ver}/R_s$). The error bar of each bin indicates bootstrap resampling uncertainty.

modulus of the Virgo cluster of 31.1 (Mei et al. 2007). Further, we construct red sequences in the $g-r$ and NUV $-$ r CMDs by a linear least-squares fitting to the early-type galaxies in the Virgo cluster (red solid lines in Figure 4). The filament galaxies show a blueward offset from the red sequence of the Virgo cluster in $g-r$; 80% (232/289) lie blueward of the -3σ deviation (red dashed line) from the Virgo red sequence in $g-r$. A more distinct offset is shown in the NUV $-$ r CMD owing to the longer baseline of NUV $-$ r color; 90% (233/259) of the filament galaxies lie blueward of the -3σ deviation (red dashed line) from the red sequence of the Virgo cluster. The NUV $-$ r CMD evidently shows that, at all magnitudes, the majority of filament galaxies occupy the region of the blue cloud as defined by galaxies in the local universe (Wyder et al. 2007, blue curve). The NUV $-$ r CMD is particularly efficient for tracing recent star formation activity because the UV flux is sensitive to young (<1 Gyr) stellar populations. This indicates that the Virgo filaments are dominated by galaxies that have experienced recent star formation.

4.2. Trends in Color and Stellar Mass

Gradients of color and stellar mass of galaxies are found in observed filaments consisting of massive galaxies with $>10^{10}\,M_\odot$; redder and more massive galaxies are closer to filaments, whereas bluer and less massive ones are found further away (e.g., Alpaslan et al. 2016; Malavasi et al. 2017; Kraljic et al. 2018; Bonjean et al. 2020; Luber et al. 2019; Sarron et al. 2019). It is intriguing to investigate whether low-mass dwarf galaxies in filaments also follow this trend.

We examined color and stellar mass distributions of filament galaxies as a function of the scaled vertical distance from the filament spine ($D_{\rm ver}/R_s$), which is defined as $D_{\rm ver}$ divided by the measured R_s of the filament. Further, we calculated mean color and mean mass for varying $D_{\rm ver}/R_s$ using the moving bin method, where the bin size and step size of $D_{\rm ver}/R_s$ are 1 and 0.4, respectively. The errors of color and mass of each bin are calculated by the bootstrap resampling method.

Figure 5 illustrates distributions of $g-r$ color (top) and stellar mass (bottom) as a function of $D_{\rm ver}/R_s$. It appears that color and stellar mass correlate with the vertical distance from the filament spine; that is, $g-r$ color becomes blue and stellar mass decreases with increasing $D_{\rm ver}/R_s$. We performed a Kolmogorov–Smirnov (K-S) test to quantify the statistical significance of this trend. We divided galaxies into two subsamples located in the inner ($0 \leqslant D_{\rm ver}/R_s \leqslant 1.75$) and outer ($1.75 < D_{\rm ver}/R_s \leqslant 3.5$) regions of the filament. The test

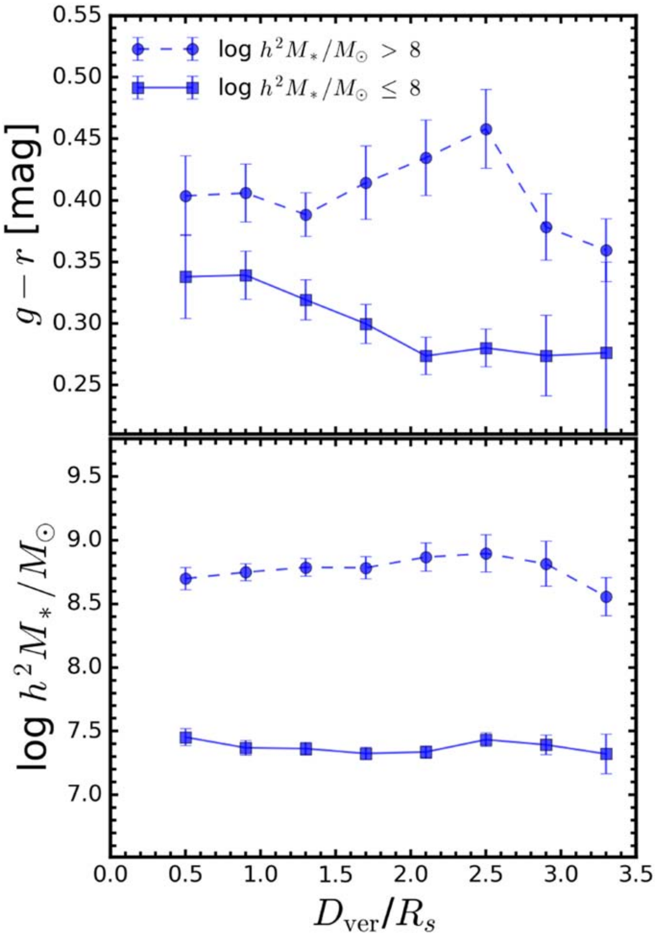

Figure 6. $g-r$ color (top) and stellar mass (bottom) vs. scaled vertical distance from the filament spine ($D_{\rm ver}/R_s$) for galaxies in different mass ranges. The circles and dashed lines represent higher-mass ($\log(h^2M_*/M_\odot) > 8$) galaxies and the squares and solid lines are lower-mass ($\log(h^2M_*/M_\odot) \leqslant 8$) galaxies. The error bar of each bin indicates bootstrap resampling uncertainty.

between two subsamples provides probabilities of 0.0312 and 0.0126 for color and stellar mass, respectively, rejecting the hypothesis that the color and stellar mass distributions between two subsamples are drawn from the same parent sample. This implies that negative gradients of color and stellar mass are evident in filaments mostly consisting of low-mass ($<10^9\,M_\odot$) dwarf galaxies. Combining this with previous results based mainly on more massive galaxies, it can be said that the color and stellar mass gradients are generally observed in the vertical direction of filaments regardless of mass range.

We divided filament galaxies into higher-mass ($\log(h^2M_*/M_\odot) > 8$) and lower-mass ($\log(h^2M_*/M_\odot) \leqslant 8$) subsamples where $\log(h^2M_*/M_\odot) = 8$ is a median stellar mass of filament galaxies. Figure 6 shows $g-r$ color and stellar mass distributions of higher-mass (circles and dashed line) and lower-mass (squares and solid line) galaxies as a function of $D_{\rm ver}/R_s$. The most notable feature is that the color distribution of higher-mass galaxies appears to be different from that of lower-mass galaxies (see top panel of Figure 6); higher-mass galaxies show a rather flat distribution, whereas the color of lower-mass galaxies appears to decrease with $D_{\rm ver}/R_s$. The K-S tests of higher- and lower-mass galaxies yield probabilities of 0.8137 and 0.0450, respectively, for color distributions between the inner ($0 \leqslant D_{\rm ver}/R_s \leqslant 1.75$) and outer ($1.75 < D_{\rm ver}/R_s \leqslant 3.5$) regions of the filament. This indicates

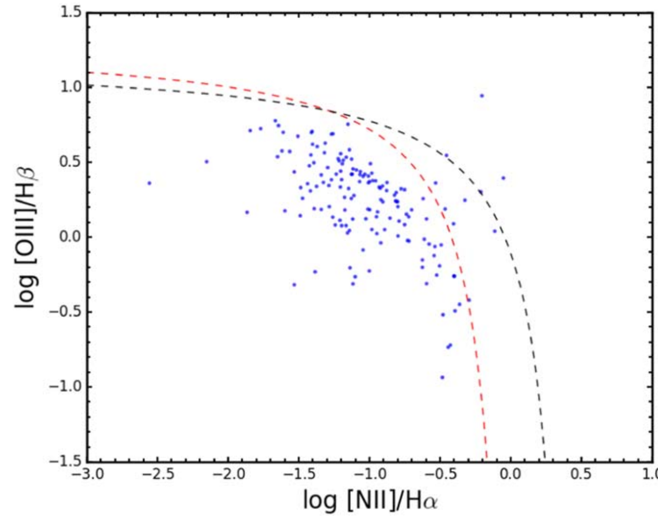

Figure 7. BPT diagram of filament galaxies. Star-forming galaxies are defined as those below the red curve of Kauffmann et al. (2003). AGNs are those above the black curve of Kewley et al. (2001).

no statistically significant difference in the color distributions of high-mass galaxies between the inner and outer regions of the filament. On the other hand, the color distribution of lower-mass galaxies closer to the filament spine shows a statistically significant difference from that of counterparts far from the filament.

In the case of stellar mass distributions, neither of the two subsamples in different mass ranges shows a significant variation of stellar mass with $D_{\rm ver}/R_s$ (see bottom panel of Figure 6). The K-S tests of higher- and lower-mass galaxies yield probabilities of 0.3187 and 0.3314, respectively, for stellar mass distributions between the inner ($0 \leqslant D_{\rm ver}/R_s \leqslant 1.75$) and outer ($1.75 < D_{\rm ver}/R_s \leqslant 3.5$) regions of the filament. This indicates that the stellar mass gradients of two subsamples are not statistically significant.

4.3. Star-forming Galaxies in Filaments

Star-forming galaxies are mostly found in less dense environments such as the field and filaments (Haines et al. 2007; Gavazzi et al. 2010). They are attractive objects for studying the degree of environmental effects in terms of their strengths of star formation. In this regard, investigation of the star formation activity of star-forming galaxies at different vertical distances from the filament spine will enable us to understand the environment of a filament.

We selected star-forming galaxies using the Baldwin–Phillips–Terlevich (BPT) emission line diagnostic diagram (Baldwin et al. 1981) that allows star-forming galaxies to be discriminated from possible active galactic nuclei (AGNs). Figure 7 is the BPT diagram where the emission line ratios [O III]/Hβ and [N II]/Hα extracted from the NSA are used. We define star-forming galaxies as those located below the empirical demarcation line of Kauffmann et al. (2003, red curve). Only galaxies with strong Hα equivalent width (i.e., EW(Hα) > 2 Å) are considered, and finally, 161 star-forming galaxies are identified. AGNs are located above the theoretical starburst model line of Kewley et al. (2001, black curve).

The Hα emission traces the ongoing star formation activity from massive stars with timescales of a few tens of millions of years. Figure 8 shows EW(Hα) distributions of higher-mass

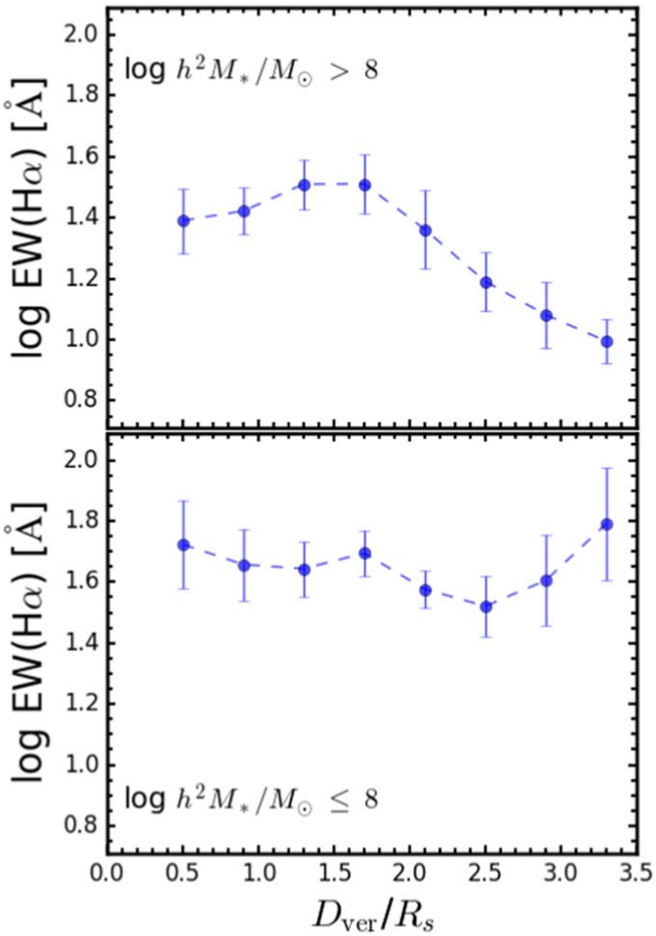

Figure 8. Equivalent width of the Hα emission line (EW(Hα)) vs. scaled vertical distance ($D_{\rm ver}/R_s$) from the filament spine of higher-mass ($\log(h^2M_*/M_\odot) > 8$) galaxies (top) and lower-mass ($\log(h^2M_*/M_\odot) \leqslant 8$) galaxies (bottom). The error bar of each bin indicates bootstrap resampling uncertainty.

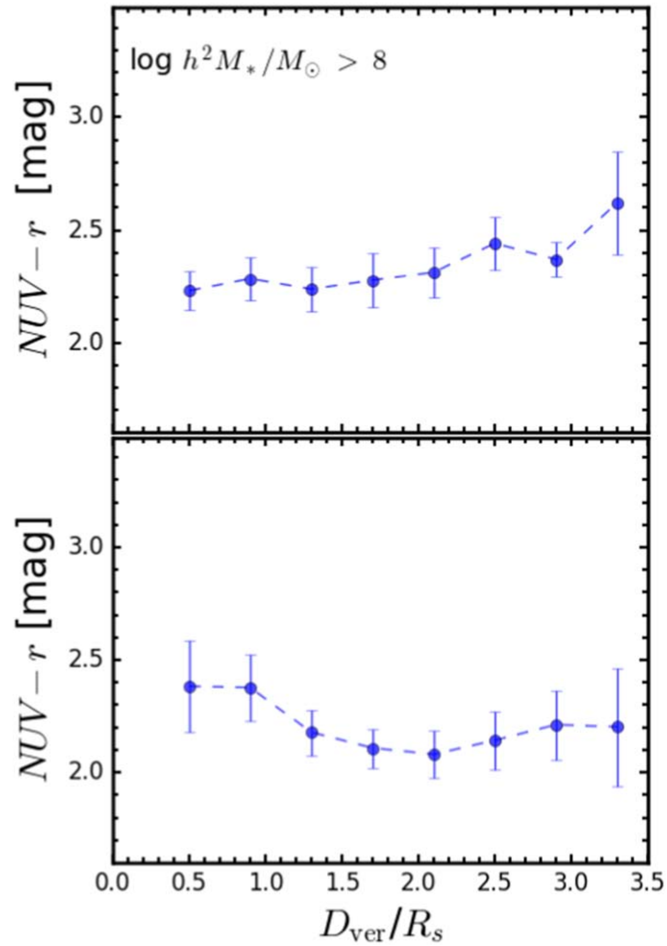

Figure 9. NUV − r color vs. scaled vertical distance ($D_{\rm ver}/R_s$) from the filament spine of higher-mass ($\log(h^2M_*/M_\odot) > 8$) galaxies (top) and lower-mass ($\log(h^2M_*/M_\odot) \leqslant 8$) galaxies (bottom). The error bar of each bin indicates bootstrap resampling uncertainty.

($\log(h^2M_*/M_\odot) > 8$, top panel) and lower-mass ($\log(h^2M_*/M_\odot) \leqslant 8$, bottom panel) galaxies as a function of $D_{\rm ver}/R_s$. The EW(Hα) distributions of the two subsamples appear to be different; the EW(Hα) values of higher-mass galaxies likely decrease with $D_{\rm ver}/R_s$, but lower-mass galaxies show no distinct trend. The K-S tests of higher- and lower-mass galaxies yield probabilities of 0.0094 and 0.5685, respectively, for EW(Hα) distributions between the inner ($0 \leqslant D_{\rm ver}/R_s \leqslant 1.75$) and outer ($1.75 < D_{\rm ver}/R_s \leqslant 3.5$) regions of the filament. This indicates that a possible EW(Hα) gradient from the filament spine is seen only for the higher-mass galaxies. We note that the EW(Hα) value from the NSA generally provides information on the central region of a galaxy due to the fiber aperture of the SDSS spectroscopic observations of 3 arcsec (i.e., 204–596 pc at a distance of 14–41 Mpc for our filaments). Therefore, current star formation in the central region of higher-mass galaxies is more active for those located closer to the filament spine.

On the other hand, the global star formation of the entire region of a galaxy can be examined by UV photometry. Figure 9 shows NUV − r color distributions of higher-mass ($\log(h^2M_*/M_\odot) > 8$, top panel) and lower-mass ($\log(h^2M_*/M_\odot) \leqslant 8$, bottom panel) galaxies as a function of $D_{\rm ver}/R_s$. The NUV − r color distribution of higher-mass galaxies is likely to show a trend of increasing very smoothly with $D_{\rm ver}/R_s$. On the other hand, the NUV − r colors of lower-mass galaxies appear to decrease with $D_{\rm ver}/R_s$. However, the K-S tests of higher- and lower-mass galaxies yield probabilities of 0.0904 and 0.0387, respectively, for NUV − r color distributions between the inner ($0 \leqslant D_{\rm ver}/R_s \leqslant 1.75$) and outer ($1.75 < D_{\rm ver}/R_s \leqslant 3.5$) regions of the filament, indicating that NUV − r color gradient is statistically significant only for lower-mass galaxies. This implies that recent (<1 Gyr) global star formation is less active in lower-mass galaxies residing closer to the filament than in their counterparts at a large displacement from the filament spine.

4.4. H I Content of Filament Galaxies

H I gas content within a galaxy has been a good tracer of different environmental effects in a cluster environment (e.g., Boselli & Gavazzi 2006). In terms of the role of the filament environment in regulating the evolution of galaxies, we also investigate the H I gas content of galaxies residing on our filaments using data from the ALFALFA (Haynes et al. 2018) blind survey. The flux limit of the ALFALFA corresponds to the detection limit of the H I mass $M_{\rm H\,I} = 10^{7.4}\,M_\odot$ at the distance of the Virgo cluster (Haynes et al. 2011, 2018). We note that owing to their proximity to us, Virgo filaments are optimal for the detection of H I gas in faint, low-mass galaxies. Of our 289 filament galaxies, 184 are included in the sky

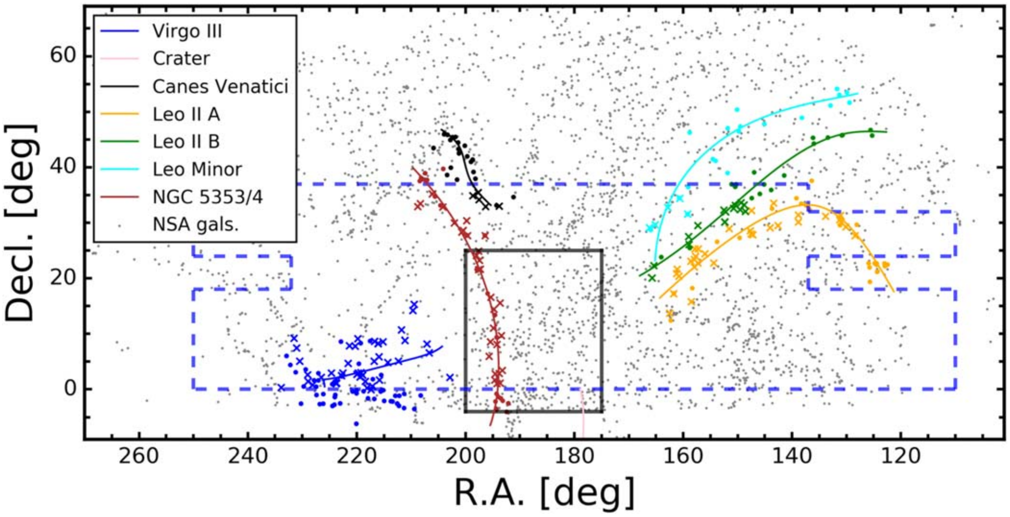

Figure 10. Spatial distribution of filament galaxies with H I detection from the ALFALFA survey data (colored crosses). Colored circles denote filament galaxies with no H I detection. Gray circles are NSA galaxies not associated with the filaments and the galaxy groups. The large rectangular box is the region of the EVCC. The coverage of the ALFALFA survey is represented by the blue dashed contour.

coverage of the ALFALFA survey (Haynes et al. 2018, see dashed contour in Figure 10), which covers the area around the Virgo cluster at declinations 0°–37°. We found that H I gas of 69% (i.e., 127) of the galaxies is detected and H I gas masses of galaxies are also extracted from the ALFALFA data. Figure 10 shows the sky distribution of galaxies with H I detection (crosses).

Figure 11 shows the distributions of H I fraction ($f_{\rm H\,I}$) of higher-mass ($\log(h^2M_*/M_\odot) > 8$, top panel) and lower-mass ($\log(h^2M_*/M_\odot) \leqslant 8$, bottom panel) galaxies as a function of $D_{\rm ver}/R_s$, where the H I fraction is defined as the ratio between H I gas mass ($M_{\rm H\,I}$) and stellar mass (M_*):

$$f_{\rm H\,I} = \log \frac{M_{\rm H\,I}}{M_*}. \tag{2}$$

At a given $D_{\rm ver}/R_s$, lower-mass galaxies have systematically higher $f_{\rm H\,I}$ than higher-mass ones. This is consistent with the general relationship between $f_{\rm H\,I}$ and stellar mass found in the Virgo cluster, in which the average gas fraction increases with decreasing stellar mass (see Figure 5 of Hallenbeck et al. 2012).

The $f_{\rm H\,I}$ distribution of higher-mass galaxies is likely to show a trend with $D_{\rm ver}/R_s$; $f_{\rm H\,I}$ decreases with increasing vertical distance from the filament spine. Lower-mass galaxies also appear to show a hint of a very smooth increase of $f_{\rm H\,I}$ with $D_{\rm ver}/R_s$. However, the K-S tests of higher- and lower-mass galaxies yield probabilities of 0.2426 and 0.4351, respectively, for $f_{\rm H\,I}$ distributions between the inner ($0 \leqslant D_{\rm ver}/R_s \leqslant 1.75$) and outer ($1.75 < D_{\rm ver}/R_s \leqslant 3.5$) regions of the filament, indicating that $f_{\rm H\,I}$ gradients of the two subsamples are not statistically significant.

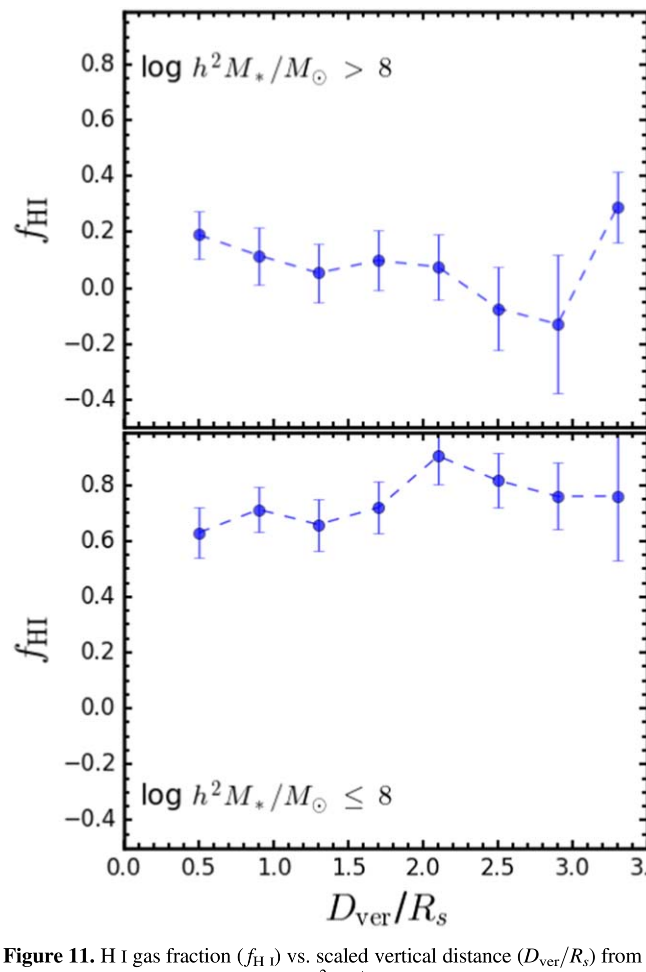

Figure 11. H I gas fraction ($f_{\rm H\,I}$) vs. scaled vertical distance ($D_{\rm ver}/R_s$) from the filament spine of higher-mass ($\log(h^2M_*/M_\odot) > 8$) galaxies (top) and lower-mass ($\log(h^2M_*/M_\odot) \leqslant 8$) galaxies (bottom). The error bar of each bin indicates bootstrap resampling uncertainty.

5. Discussion

In the filament structures around the Virgo cluster, which are mostly composed of faint, low-mass ($\log(h^2M_*/M_\odot) < 9$) galaxies, we observe negative stellar mass and $g - r$ color gradients in the vertical direction of filaments (see Figure 5). These features are also found in previous results based on the sample of massive galaxies in more distant filaments (Mahajan et al. 2018; Luber et al. 2019; Sarron et al. 2019); galaxies closer to the filament spine have higher stellar masses and redder colors than those further from the filaments. A generally suggested mechanism for this mass gradient is galaxy mergers in the past (Malavasi et al. 2017; Kraljic et al. 2018), in which more massive galaxies finish their assembly of stellar mass closer to the filament spine owing to a higher merger rate (Dubois et al. 2014). The formation of these massive merger remnants is accompanied by subsequent changes in their colors since the mass regulates properties of galaxies (Peng et al. 2010). This is in line with the suggestion that mass is the main parameter driving galaxy properties in filaments (e.g., Robotham et al. 2013; Alpaslan et al. 2015, 2016).

Interestingly, when we narrow down the mass ranges of galaxies by dividing them into two subsamples (i.e., higher-mass with $\log(h^2 M_*/M_\odot) > 8$ and lower-mass with $\log(h^2 M_*/M_\odot) \leqslant 8$), no mass gradient is observed for either mass range (see bottom panel of Figure 6). In this case, color gradients are also not anticipated in terms of the connection between stellar mass and color of galaxies. This is shown for higher-mass galaxies; stellar mass and the color of higher-mass galaxies are almost statistically invariant with the vertical distance from the filament spine. However, in the case of lower-mass galaxies, the overall feature of the color distribution is decoupled from the stellar mass distribution; although stellar masses of galaxies are similar for all distances, the negative color gradient is clearly displayed (see top panel of Figure 6). This indicates that an additional process might be responsible for the color gradient shown in lower-mass galaxies.

The local environment is generally considered as the second parameter in determining galaxy properties at fixed stellar mass (e.g., Peng et al. 2010; Geha et al. 2012; Wetzel et al. 2012). In this regard, the interaction between galaxies is thought to be one of the typical environmental processes. The strong tidal forces in interacting galaxies can remove a large amount of gas from the outer part of galaxies, leading to a subsequent decrease in global star formation activity (Barnes & Hernquist 1991; Mihos & Hernquist 1994, 1996; Di Matteo et al. 2007). Meanwhile, galaxy interaction also causes funneling of gas into the central region of galaxies, which could trigger strong central bursts of star formation (Barnes & Hernquist 1996; Mihos & Hernquist 1996; Kewley et al. 2006).

The NUV $-$ r color distribution of lower-mass galaxies shows a clear negative correlation with the distance from the filament spine (see Figure 9), indicating that global star formation is depressed for lower-mass galaxies residing toward the filament spine. This is consistent with a general prediction that the efficiency of galaxy interaction could decrease moving further away from the filament spine. However, contrary to an expectation of gas flows toward the central region by galaxy interaction, lower-mass galaxies show no distinct variation of central star formation, traced by EW(Hα), with the distance from the filament spine (see Figure 8); i.e., lower-mass galaxies closer to the spine do not show enhanced central star formation. The gravitational restoring force of a lower-mass galaxy to retain an interstellar medium could be very small due to its shallow potential well. If the tidal force exerted by a companion galaxy is greater than the restoring force of the lower-mass galaxy, a large fraction of its gaseous material would be perturbed and then removed. Therefore, the EW(Hα) distribution of lower-mass galaxies could be explained by a lack of available fuel infalling from the outskirts of galaxies for their central star formation.

In the case of higher-mass galaxies with deep potential wells, much of the original gas reservoir is likely to be retained against the tidal force of the interaction. Our result clearly indicates that global star formation of higher-mass galaxies is not sensitive to the galaxies' distance from the filament spine (see Figure 9). In this case, on the other hand, higher-mass galaxies residing closer to the filament spine would show an enhancement in central star formation by funneling a large quantity of available gas into the central region of the galaxies (see Figure 8).

An environmental mechanism related to the intergalactic medium, such as ram pressure stripping, is important for regulating star formation and the evolution of galaxies in galaxy clusters (e.g., Gunn & Gott 1972; Larson et al. 1980). Benítez-Llambay et al. (2013) also show that hydrodynamical interaction between a galaxy and intergalactic gas in the filaments results in the removal of much of the gaseous component within a galaxy when the galaxy traverses the filaments. Therefore, ram pressure stripping in the filament, the so-called "cosmic-web stripping" (Benítez-Llambay et al. 2013), is also expected to potentially influence the properties of galaxies in the filament environment (Sancisi et al. 2008; Aragon Calvo et al. 2019). Numerical simulations and X-ray observations might support this idea such that filaments host WHIM as the dominant baryon mass contribution in filaments (e.g., Eckert et al. 2015; Akamatsu et al. 2017; Parekh et al. 2017; Martizzi et al. 2019; Tanimura et al. 2019).

The ram pressure stripping can be probed by the H I cold gas content within galaxies. In this regard, Luber et al. (2019) found a positive gradient of H I fraction in galaxies with a mean stellar mass of $10^{10}\,M_\odot$, in which galaxies further away from the filaments show a higher H I fraction, indicating that H I gas in galaxies closer to filaments can be efficiently removed by a process related to the intrafilament medium. The deprivation of gas in galaxies would be more pronounced in low-mass galaxies due to their shallower potential wells. However, in the case of our lower-mass ($\log(h^2 M_*/M_\odot) \leqslant 8$) subsample, the difference in H I fraction distributions between the inner and outer regions of the filament is not statistically significant (see Figure 11). This implies that the ram pressure stripping does not play a significant role in reducing the H I gas of lower-mass galaxies in filaments. It might be tempting to ascribe the lack of a distinct gradient of H I fraction in filament galaxies to the intrinsic property of the intergalactic medium in the Virgo filaments characterized by a low density of WHIM.

In terms of understanding galaxy evolution in filaments, it can be said that galaxies can replenish H I gas content through cold-mode gas accretion from the filaments (Kereš et al. 2005 and references therein; Kleiner et al. 2017). This is supported by numerical simulations that also show that filaments host diffuse H I gas at low redshift (e.g., Popping et al. 2009). Kleiner et al. (2017) found tentative evidence of cold gas accretion for massive galaxies with stellar masses of $>10^{11}\,M_\odot$ from the intrafilament medium, whereas no hint of gas accretion was observed for low-mass galaxies with $<10^{11}\,M_\odot$. They proposed that cold-mode gas accretion is only allowed for the most massive galaxies in filaments owing to the larger gravitational potentials of galaxies that are sufficient to pull cold gas from the intrafilament medium. The difference in H I fraction of our higher-mass galaxies between the inner and outer regions of the filament is not found to be statistically significant (see Figure 11), indicating the absence of any gas accretion. Our result is in line with that of Kleiner et al. (2017), considering that the mass range of our higher-mass galaxies ($\log(h^2 M_*/M_\odot) \sim 8$–11) corresponds to that of their low-mass galaxies.

6. Summary and Conclusions

In this study, we have explored the properties of galaxies in six filaments around the Virgo cluster, which are the nearest large-scale structures to us (∼14–41 Mpc), as a function of the vertical distance from the filament spine. Using the NSA and galaxy group catalogs, we selected galaxies that do not belong to galaxy groups in filaments and defined filament member galaxies that are located within 3.5 scale length from the filament spine. The main results are the following.

1. The filaments are mainly composed of low-mass dwarf galaxies; the median value of the stellar mass distribution is $\log(h^2M_*/M_\odot) = 7.7$ and 87% of the total sample have stellar mass $\log(h^2M_*/M_\odot) < 9$. In $g - r$ and NUV $- r$ CMDs, the filament galaxies show a blueward offset from the red sequence of the Virgo cluster and are dominantly located on the blue cloud.
2. We observe that $g - r$ color and stellar mass correlate with the vertical distance from the filament spine; color becomes blue and stellar mass decreases with increasing vertical filament distance. We confirm that these trends are statistically significant in the K-S test between two subsamples located in the inner and outer regions of the filament. We propose that the negative color and stellar mass gradients of galaxies found in our filaments can be explained by mass assembly depending on the efficiency of galaxy mergers at different vertical distances from the filament spine and subsequent changes in their colors regulated by final mass.
3. We also examined the $g - r$ color and stellar mass distributions of galaxy subsamples in different mass ranges: higher-mass galaxies with $\log(h^2M_*/M_\odot) > 8$ and lower-mass galaxies with $\log(h^2M_*/M_\odot) \leqslant 8$. The $g - r$ color distribution of higher-mass galaxies is found to be different from that of lower-mass galaxies; higher-mass galaxies have a flat distribution with the vertical filament distance, whereas lower-mass galaxies show a clear negative color gradient. In the case of stellar mass distribution, no significant trend of stellar mass with the vertical filament distance is shown by either subsample in different mass ranges.
4. We inspected EW(Hα) and NUV $- r$ color distributions of higher- and lower-mass subsamples, which trace central and global star formation activities of galaxies, respectively, using star-forming galaxies selected by the BPT emission line diagnostic diagram. The EW(Hα) distributions in the two subsamples are different: we observe a negative EW(Hα) gradient for higher-mass galaxies, whereas lower-mass galaxies show no distinct variation of EW(Hα). On the other hand, NUV $- r$ color distributions exhibit the opposite trend in different mass ranges; the NUV $- r$ color distribution of higher-mass galaxies shows no statistically strong dependence on the vertical filament distance, but lower-mass galaxies show a distinct negative NUV $- r$ color gradient. All the observed EW(Hα) and NUV $- r$ color distributions of higher- and lower-mass subsamples can be qualitatively explained by different star formation efficiency in galaxy interactions depending on the masses of galaxies.
5. We observe no clear trend in the distributions of H I fraction for two subsamples detected from the ALFALFA blind survey data. Both higher- and lower-mass galaxies show no statistically significant variations in H I fractions with the vertical filament distance. This indicates that possible mechanisms related to the intrafilament medium, such as ram pressure stripping and gas accretion, may be ignored for galaxies in the Virgo filaments. Although the ALFALFA data obtained from the Arecibo single-dish telescope provide us a statistical view of the gas content of galaxies, further deep H I surveys using more sensitive telescopes in very large arrays will improve our understanding of the H I content of galaxies within the Virgo filaments.

We are grateful to the anonymous referee for helpful comments and suggestions that improved the clarity and quality of this paper. Y.D.L., acting as the corresponding author, acknowledges support from Basic Science Research Program through the National Research Foundation of Korea (NRF) funded by the Ministry of Education (2020R1A6A3A01099777). S.C.R., acting as the corresponding author, acknowledges support from the Basic Science Research Program through the National Research Foundation of Korea (NRF) funded by the Ministry of Education (2018R1A2B2006445). Support for this work was also provided by the NRF to the Center for Galaxy Evolution Research (2017R1A5A1070354). S.K. acknowledges support from the Basic Science Research Program through the National Research Foundation of Korea (NRF) funded by the Research Staff Program (NRF-2019R1I1A1A01061237).

ORCID iDs

Youngdae Lee https://orcid.org/0000-0002-6261-1531
Suk Kim https://orcid.org/0000-0002-3738-885X
Soo-Chang Rey https://orcid.org/0000-0002-0041-6490
Jiwon Chung https://orcid.org/0000-0003-0469-345X

References

Aguerri, J. A. L., Gerhard, O. E., Arnaboldi, M., et al. 2005, AJ, 129, 2585
Akamatsu, H., Fujita, Y., Akahori, T., et al. 2017, A&A, 606, A1
Alpaslan, M., Driver, S., Robotham, A. S. G., et al. 2015, MNRAS, 451, 3249
Alpaslan, M., Grootes, M., Marcum, P. M., et al. 2016, MNRAS, 457, 2287
Aragon Calvo, M. A., Neyrinck, M. C., & Silk, J. 2019, OJAp, 2, 7
Baldwin, J. A., Phillips, M. M., & Terlevich, R. 1981, PASP, 93, 5
Barnes, J. E., & Hernquist, L. 1996, ApJ, 471, 115
Barnes, J. E., & Hernquist, L. E. 1991, ApJL, 370, L65
Benítez-Llambay, A., Navarro, J. F., Abadi, M. G., et al. 2013, ApJL, 763, L41
Bond, J. R., Kofman, L., & Pogosyan, D. 1996, Natur, 380, 603
Bonjean, V., Aghanim, N., Douspis, M., Malavasi, N., & Tanimura, H. 2020, A&A, 638, A75
Boselli, A., & Gavazzi, G. 2006, PASP, 118, 517
Chen, Y.-C., Ho, S., Mandelbaum, R., et al. 2017, MNRAS, 466, 1880
Cybulski, R., Yun, M. S., Fazio, G. G., & Gutermuth, R. A. 2014, MNRAS, 439, 3564
Darvish, B., Mobasher, B., Sobral, D., et al. 2015, ApJ, 814, 84
Davies, L. J. M., Robotham, A. S. G., Driver, S. P., et al. 2015, MNRAS, 452, 616
De Lucia, G., Weinmann, S., Poggianti, B. M., Aragón-Salamanca, A., & Zaritsky, D. 2012, MNRAS, 423, 1277
Di Matteo, P., Combes, F., Melchior, A. L., & Semelin, B. 2007, A&A, 468, 61
Dubois, Y., Pichon, C., Welker, C., et al. 2014, MNRAS, 444, 1453
Eckert, D., Jauzac, M., Shan, H., et al. 2015, Natur, 528, 105
Fujita, Y. 2004, PASJ, 56, 29
Gavazzi, G., Fumagalli, M., Cucciati, O., & Boselli, A. 2010, A&A, 517, A73
Geha, M., Blanton, M. R., Yan, R., & Tinker, J. L. 2012, ApJ, 757, 85
Gunn, J. E., & Gott, J. R., III 1972, ApJ, 176, 1
Haines, C. P., Gargiulo, A., La Barbera, F., et al. 2007, MNRAS, 381, 7
Hallenbeck, G., Papastergis, E., Huang, S., et al. 2012, AJ, 144, 87

Haynes, M. P., Giovanelli, R., Kent, B. R., et al. 2018, ApJ, 861, 49
Haynes, M. P., Giovanelli, R., Martin, A. M., et al. 2011, AJ, 142, 170
Karachentsev, I. D., & Makarov, D. A. 1996, AJ, 111, 794
Kauffmann, G., Heckman, T. M., Tremonti, C., et al. 2003, MNRAS, 346, 1055
Kereš, D., Katz, N., Weinberg, D. H., & Davé, R. 2005, MNRAS, 363, 2
Kewley, L. J., Dopita, M. A., Sutherland, R. S., Heisler, C. A., & Trevena, J. 2001, ApJ, 556, 121
Kewley, L. J., Geller, M. J., & Barton, E. J. 2006, AJ, 131, 2004
Kim, S., Rey, S.-C., Bureau, M., et al. 2016, ApJ, 833, 207
Kim, S., Rey, S.-C., Jerjen, H., et al. 2014, ApJS, 215, 22
Kleiner, D., Pimbblet, K. A., Jones, D. H., Koribalski, B. S., & Serra, P. 2017, MNRAS, 466, 4692
Komatsu, E., Smith, K. M., Dunkley, J., et al. 2011, ApJS, 192, 18
Kraljic, K., Arnouts, S., Pichon, C., et al. 2018, MNRAS, 474, 547
Kuutma, T., Tamm, A., & Tempel, E. 2017, A&A, 600, L6
Larson, R. B., Tinsley, B. M., & Caldwell, C. N. 1980, ApJ, 237, 692
Luber, N., van Gorkom, J. H., Hess, K. M., et al. 2019, AJ, 157, 254
Mahajan, S. 2013, MNRAS, 431, L117
Mahajan, S., Singh, A., & Shobhana, D. 2018, MNRAS, 478, 4336
Malavasi, N., Arnouts, S., Vibert, D., et al. 2017, MNRAS, 465, 3817
Martínez, H. J., Muriel, H., & Coenda, V. 2016, MNRAS, 455, 127
Martizzi, D., Vogelsberger, M., Artale, M. C., et al. 2019, MNRAS, 486, 3766
Mei, S., Blakeslee, J. P., Côté, P., et al. 2007, ApJ, 655, 144
Mihos, J. C., & Hernquist, L. 1994, ApJL, 431, L9
Mihos, J. C., & Hernquist, L. 1996, ApJ, 464, 641
Parekh, V., Durret, F., Padmanabh, P., & Pandge, M. B. 2017, MNRAS, 470, 3742
Peng, Y.-j., Lilly, S. J., Kovač, K., et al. 2010, ApJ, 721, 193
Popping, A., Davé, R., Braun, R., & Oppenheimer, B. D. 2009, A&A, 504, 15
Praton, E. A., & Schneider, S. E. 1994, ApJ, 422, 46
Robotham, A. S. G., Liske, J., Driver, S. P., et al. 2013, MNRAS, 431, 167
Sancisi, R., Fraternali, F., Oosterloo, T., & van der Hulst, T. 2008, A&ARv, 15, 189
Sarron, F., Adami, C., Durret, F., & Laigle, C. 2019, A&A, 632, A49
Springel, V., White, S. D. M., Jenkins, A., et al. 2005, Natur, 435, 629
Tanimura, H., Hinshaw, G., McCarthy, I. G., et al. 2019, MNRAS, 483, 223
Tonnesen, S., Bryan, G. L., & van Gorkom, J. H. 2007, ApJ, 671, 1434
Vulcani, B., Poggianti, B. M., Oemler, A., et al. 2013, A&A, 550, A58
Wetzel, A. R., Tinker, J. L., & Conroy, C. 2012, MNRAS, 424, 232
Wyder, T. K., Martin, D. C., Schiminovich, D., et al. 2007, ApJS, 173, 293
Zabludoff, A. I., Zaritsky, D., Lin, H., et al. 1996, ApJ, 466, 104